

On oblique and parallel shedding behind an inclined plate

Dan Yang, Bjørnar Pettersen, Helge I. Andersson, and Vagesh D. Narasimhamurthy

Citation: *Phys. Fluids* **25**, 054101 (2013); doi: 10.1063/1.4802046

View online: <http://dx.doi.org/10.1063/1.4802046>

View Table of Contents: <http://pof.aip.org/resource/1/PHFLE6/v25/i5>

Published by the [American Institute of Physics](#).

Additional information on Phys. Fluids

Journal Homepage: <http://pof.aip.org/>

Journal Information: http://pof.aip.org/about/about_the_journal

Top downloads: http://pof.aip.org/features/most_downloaded

Information for Authors: <http://pof.aip.org/authors>

ADVERTISEMENT



**Running in Circles Looking
for the Best Science Job?**

Search hundreds of exciting
new jobs each month!

<http://careers.physicstoday.org/jobs>

physicstoday JOBS



On oblique and parallel shedding behind an inclined plate

Dan Yang,^{1,a)} Bjørnar Pettersen,¹ Helge I. Andersson,²
 and Vagesh D. Narasimhamurthy²

¹*Department of Marine Technology, Norwegian University of Science and Technology, Trondheim NO-7491, Norway*

²*Department of Energy and Process Engineering, Norwegian University of Science and Technology, Trondheim NO-7491, Norway*

(Received 24 September 2012; accepted 28 March 2013; published online 1 May 2013)

Three-dimensional wake instabilities in the form of oblique shedding and vortex dislocations in the flow past an inclined flat plate of angle of attack 20° and Reynolds number 1000 have been reported earlier [D. Yang, B. Pettersen, H. I. Andersson, and V. D. Narasimhamurthy, *Phys. Fluids* **24**, 084103 (2012)]. In the current study, direct numerical simulations were performed to further explore this bifurcation. At lower Reynolds numbers, i.e., well below 525, the three-dimensional wake was found to be stable and in a parallel shedding mode. However, as the Reynolds number increases, it was observed that both parallel and oblique vortex sheddings arose naturally. Vortex dislocations appeared at the juxtaposition of oblique and parallel shedding modes. The velocity signals were analyzed by a wavelet transformation, from which the instantaneous characteristics of three-dimensional vortex shedding were obtained and examined. Results show that the phase difference of shed vortex rollers in the spanwise direction gave a symmetric probability density function. This indicates that both positive and negative shedding angles (relative to the axis of the plate) occur with equal likelihood. © 2013 AIP Publishing LLC. [<http://dx.doi.org/10.1063/1.4802046>]

I. INTRODUCTION

The complex physical phenomena related to the three-dimensional wakes of bluff bodies have been investigated considerably. According to Roshko,¹ the three-dimensionality of the wake flows was attributed both to extrinsic (generated by extraneous effects) and intrinsic (generated naturally) factors.

In the wake of circular cylinders, in the Reynolds number range of ~ 50 – 150 , a common observation was made in the experiments that the axes of the shed vortices were not parallel to the cylinder axis (Eisenlohr and Eckelmann² and Williamson³). The phenomenon of the oblique laminar vortex shedding, known as a three-dimensional effect (Williamson⁴), was controlled to some extent by the end conditions. The oblique shedding causes a discontinuity in the curve of Strouhal number (St) versus Reynolds number (Re). By manipulating the end plates, parallel shedding modes were obtained and the oblique shedding frequencies were found to be lower when compared to the parallel shedding frequencies. Introducing a numerical no-slip boundary condition on one of the sidewalls along the span resulted in oblique vortex shedding in the laminar flow regime, $Re = 60 - 150$ (Behara and Mittal⁵). Cellular shedding was observed and spotlike vortex dislocations were formed at the junction of the cells.

In the wake transition regime, the $St - Re$ curve involves two discontinuities corresponding to the three-dimensional “mode A” and “mode B” at $Re = 190$ and $Re = 230$ – 260 , respectively (Williamson⁶). These two modes have spanwise wavelengths of four and one diameters, respectively. The three-dimensional wake transition involves not only small-scale structures but also surprisingly

^{a)} dan.yang@ntnu.no

large structures such as spotlike vortex dislocations, which can emerge naturally. By introducing a small disturbance at a local spanwise position, Williamson⁷ produced vortex dislocations artificially in a laminar wake ($Re = 120$).

Karniadakis and Triantafyllou⁸ first observed a period-doubling in the near wake of a circular cylinder at $Re = 300$ in their direct numerical simulations. Another one was discovered at $Re = 333$. As the Reynolds number increased to 500, a chaotic behavior and spectral broadening characteristics of turbulent flow were observed. Williams *et al.*⁹ found subharmonic modes produced by the intrinsic three-dimensional instability when the Reynolds number exceeded 300. These subharmonics observed in their experiments were proven to be consistent with the period-doubling route to transition in the simulations of Karniadakis and Triantafyllou.⁸ Mittal and Balachandar¹⁰ also detected the subharmonics at $Re = 525$. These subharmonic modes were shown in association with the hairpin vortex structures in their direct numerical simulations. In the simulation by Henderson,¹¹ the large scale of phase dislocations appeared spontaneously in the near wake, which he described as “turbulent spots” at $Re = 1000$.

Other three-dimensional flow phenomena of different types appear in the wakes, as reported by Yang *et al.*¹² and Mansy *et al.*¹³ Structures of low-frequency vortex dislocations in the wake of a circular cylinder were reported by Yang *et al.*¹² The origin of these vortex dislocations was shown as the superposition of two waves with slightly different frequencies. The higher and lower frequencies corresponded to the parallel and oblique waves, respectively.

Miau *et al.*^{14–16} explored the low-frequency behavior of vortex shedding behind a bluff body at Re between 1800 and 27 000. The velocity measurements obtained simultaneously at different spanwise locations in their experiments allowed for the linkage between the spanwise phase differences of shedding vortices and low-frequency modulations embedded in the vortex shedding signals examined (see also Wu *et al.*¹⁷).

As mentioned before, the vortex dislocations and the oblique vortex shedding can be observed by introducing non-uniform conditions along the span. The wakes of bluff bodies with relatively simple cross-sectional variations, such as tapered and stepped cylinders, which are subjected to uniform or non-uniform inflow, have been investigated by many researchers (Lewis and Gharib,¹⁸ Hsiao and Chiang,¹⁹ Mittal,²⁰ Narasimhamurthy *et al.*,^{21,22} Ling and Zhao,²³ Morton and Yarusevych,²⁴ Huang *et al.*,²⁵ and Dunn and Tavoularis²⁶). The roles of oblique shedding, vortex dislocations, frequency discontinuity, and phase difference in the spanwise direction were studied, and the relationship among these three-dimensional wake phenomena was discussed.

Bailey *et al.*²⁷ investigated the three-dimensional vortex shedding from a square cylinder in the vicinity of a solid wall as a function of the gap height at $Re = 18\,900$. They observed that the parallel and oblique shedding modes arise naturally. The number of vortex dislocations, which were strongly associated with “mode A” instability and vortex splitting, were related to the variations in the oblique shedding angle.

Flow past an inclined or normal flat plate is a common configuration which also has been investigated extensively. In the short review of Thompson *et al.*,²⁸ the flow past a flat plate with width d normal to the flow undergoes a transition to the two unstable modes at a Reynolds number around 105–110 and 125, with wavelengths of $\sim 5–6d$ and $2d$ for the two modes.

Recently, the present authors (Yang *et al.*²⁹) made simulations of flow past an inclined flat plate at angles of attack $\alpha = 20–30^\circ$. The results showed that the vortex shedding frequency was not constant along the span of the plate for one of the incidence angles. Oblique shedding and vortex dislocations were observed in the wake at $\alpha = 20^\circ$ and $Re = 1000$. It was demonstrated that these three-dimensional effects are associated with the angle of attack (Yang *et al.*²⁹). Lam and Leung³⁰ also pointed out that in their experiments with a flat plate, at angle of attack $\alpha = 20^\circ$ and 25° , the spectral peaks were not as sharp as expected for regular vortex shedding from other bluff bodies. This phenomenon was particularly clear as $Re < 10\,000$. They observed that natural vortex shedding from a stationary plate at high angle of incidence was impaired with poor periodicity and poor regularity, which was due to the increasing degree of three-dimensionality of the wake (Perry and Steiner³¹).

The aim of the present study is to explore in detail the vortex shedding characteristics behind a flat plate inclined at $\alpha = 20^\circ$ at Reynolds numbers for which the wake is distinctly three-dimensional.

This is motivated by observations made in our preceding study (Yang *et al.*²⁹) of vortex shedding behind flat plates at attack angles from 20° to 30° at Reynolds number $Re = 1000$. In spite of the uniformity of the width d of the plate and the use of periodic rather than no-slip conditions in the spanwise direction, oblique vortex shedding was observed for $\alpha = 20^\circ$ and was accompanied by vortex dislocations. However, the shedding mode alternated between an oblique shedding mode and the conventional parallel shedding. At that time we conjectured that the unexpected occurrence of oblique vortex shedding was due to the relatively low incidence angle rather than the actual value of the Reynolds number. In the present investigation, this hypothesis will be addressed by means of three-dimensional flow simulations in the intermediate range of Reynolds numbers from 400 to 600. Furthermore, if oblique vortex shedding occurs, the wake topology will be explored in detail by various means in order to better comprehend the phenomenon.

II. PROBLEM FORMULATION AND COMPUTATIONAL APPROACH

The governing equations for the flow past an inclined flat plate are the unsteady incompressible Navier-Stokes equations. The equations are written in a general Cartesian coordinate system and are normalized by the plate width d and the uniform upstream velocity U_0 . The non-dimensional form of the equations is expressed as

$$\frac{\partial u_i}{\partial x_i} = 0, \quad (1)$$

$$\frac{\partial u_i}{\partial t} + u_j \frac{\partial u_i}{\partial x_j} = -\frac{\partial p}{\partial x_i} + \frac{1}{Re} \frac{\partial^2 u_i}{\partial x_j \partial x_j}. \quad (2)$$

The indices i, j refer to the streamwise (x), spanwise (y), and transverse (z) direction, respectively. The Reynolds number is defined as $Re = U_0 d / \nu$.

The computational procedure for solving the full three-dimensional Navier-Stokes equations for an incompressible fluid is summarized as follows. The finite volume solver MGLET (Manhart³²) for non-uniform Cartesian grids, on which the dependent variables are arranged staggered, is used. The spatial discretization is based on second-order central differences. The discretized momentum equations are advanced in time by fractional time stepping using a third-order Runge-Kutta scheme. The Poisson equation for the pressure correction is solved by the strongly implicit procedure (SIP) by Stone.³³

For the representation of the flat plate, an immersed boundary technique is used. The plate geometry is represented by a triangular mesh and the interface cells are searched in a pre-processing algorithm. The immersed boundary technique provides a smooth representation of the body surface by using third-order least squares interpolation for the interface cells (Peller *et al.*³⁴).

The computational domain is $25d \times 15d$ in streamwise and transverse direction, with the plate centre located a distance $5d$ from the inlet. The number of grid points is 672×450 . The computational domain and grid resolution used in the streamwise and transverse direction are carefully based on a previous study performed by the present authors (Yang *et al.*^{29,35}). A uniform free stream velocity is assumed at the inlet. The Neumann boundary condition is used at the outlet boundary. At the top and bottom boundaries, the free-slip condition is adopted. In the spanwise direction, periodic boundary conditions are imposed. The no-slip condition is prescribed on the plate surface.

In order to assess the influence of spanwise resolution on the results, a flow at $Re = 600$ has been studied and the results are presented in Table I. The numerical results for flow past a flat plate inclined at $\alpha = 18^\circ$ and $Re = 20\,000$, by Breuer and Jovičić,³⁶ are also shown in Table I. First of all it is noteworthy that both the drag and lift coefficients are over-predicted in two-dimensional simulations as compared with the more realistic 3D simulations. This finding is fully consistent with the earlier observation by Breuer and Jovičić³⁶ at a significantly higher Reynolds number.

For the same spanwise length $6d$, the number of nodes, N_y , are 72 and 108. The drag and lift coefficients in the two lower rows in Table I show very small differences. In addition, the pressure coefficient, defined by $\bar{C}_p = 2(\bar{p} - p_0) / \rho U_0^2$, is also compared for the two grids in Figs. 1(a) and 1(b). The two contour plots are almost indistinguishable. The three-dimensional vortex structures

TABLE I. Influence of spanwise length L_y and resolution N_y on integral parameters \bar{C}_D and \bar{C}_L . Data from a large-eddy simulation study by Breuer and Jovičić³⁶ are included for comparison.

| Method | Dimension | α (deg) | Re | L_y | N_y | \bar{C}_D^a | \bar{C}_L^b |
|---|-----------|----------------|--------|-------|-------|---------------|---------------|
| LES (Breuer and Jovičić ³⁶) | 2D | 18 | 20 000 | ... | ... | 0.57 | 1.69 |
| LES (Breuer and Jovičić ³⁶) | 3D | 18 | 20 000 | d | 72 | 0.38 | 1.12 |
| Present DNS | 2D | 20 | 550 | ... | ... | 0.457 | 1.017 |
| Present DNS | 3D | 20 | 550 | $6d$ | 72 | 0.424 | 0.931 |
| Present DNS | 3D | 20 | 550 | $9d$ | 108 | 0.420 | 0.920 |
| Present DNS | 2D | 20 | 600 | ... | ... | 0.454 | 1.022 |
| Present DNS | 3D | 20 | 600 | $6d$ | 72 | 0.412 | 0.910 |
| Present DNS | 3D | 20 | 600 | $6d$ | 108 | 0.414 | 0.913 |

^a $\bar{C}_D = 2F_D / (\rho U_0^2 d)$, where F_D is the drag force.

^b $\bar{C}_L = 2F_L / (\rho U_0^2 d)$, where F_L is the lift force.

are compared in Figs. 1(c) and 1(d) and it is shown that the different grid resolutions do not affect the spanwise modulation which is of our concern here. The two instantaneous vorticity fields exhibit the same topology of the shed vortex cells visualized by means of ω_y -contours. The instantaneous ω_x -contours furthermore demonstrate that the streamwise-oriented vortices are adequately resolved on both grids.

Comparisons are also made with a larger spanwise length, $L_y = 9d$, with the same grid resolution at $Re = 550$ in order to check the effect of the spanwise domain size. No significant differences can be found in the integral parameters, i.e., drag and lift coefficients (Table I). Hence, the three-dimensional calculations in this study are carried out with spanwise length $6d$ and 72 nodes. Further numerical details can be found in Yang *et al.*³⁵

III. RESULTS AND DISCUSSION

In this paper results from three-dimensional computer simulations are presented for wake flow behind a flat plate inclined at $\alpha = 20^\circ$ with respect to the uniform inflow. In Subsection III A the focus is on Reynolds number effects on the instantaneous flow field in the transition range from $Re = 400$ to 600. The three-dimensional wake dynamics at $Re = 550$ are subjected to a wavelet analysis in Subsection III B and spanwise phase differences are reported in Subsection III C.

A. The natural three-dimensional vortex pattern

The three-dimensional wake transition characteristics behind an inclined flat plate at $\alpha = 25^\circ$ were investigated by Yang *et al.*³⁵ The secondary vortex structures start to develop in the Re range 275–300 and the flow field becomes three-dimensional. To understand how the three-dimensional structures develop with increasing Reynolds number at $\alpha = 20^\circ$ in the wake transition regime, the present study starts at the fairly low Reynolds number $Re = 400$. Regular vortex structures were detected in the Re range of 400–450. As shown in Fig. 2, the organized counter-rotating “braid”-like structures appear at $Re = 450$ and $Re = 500$. A perspective view of the spanwise vorticity field in the near wake at $Re = 500$ is shown in Fig. 2(c) where the three-dimensionality can easily be observed in the near wake.

In the simulations of Yang *et al.*³⁵ at $\alpha = 25^\circ$, the organized spanwise wavelength at $Re = 350$ was $0.708d$, while in the present study at $Re = 450$ and $Re = 500$, the spanwise wavelength is $0.67d$ and $0.75d$, respectively. This could be clearly observed in the spanwise evolution of the transverse velocity component w in Fig. 3.

In the present paper, the velocity and pressure signals are sampled at $x/d = 6.0$ and $z/d = 8.0$ to perform time-frequency analysis. The frequency spectra of the transverse velocity component display a spanwise oscillation with a regular wavelength, as shown in Fig. 4. Here, the primary frequency $fd/U_0 = 0.5188$ is associated with the shedding of the spanwise-oriented von Kármán

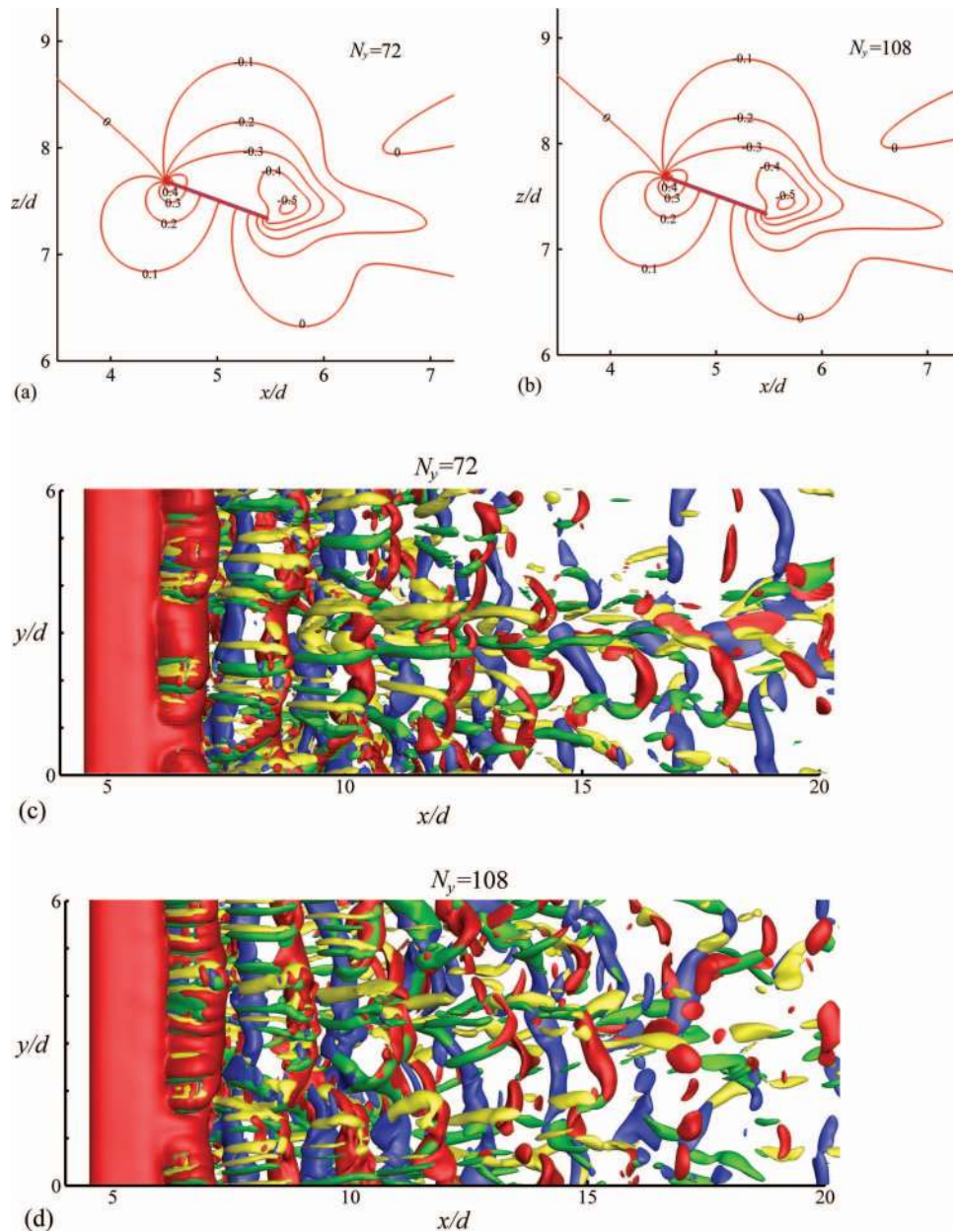


FIG. 1. Pressure coefficient \bar{C}_p contours around the plate at $Re = 600$ and $L_y = 6d$ with different spanwise resolutions, (a) $N_y = 72$ nodes and (b) $N_y = 108$ nodes. Instantaneous iso-vorticity surfaces, $\omega_x = \pm 1$ (yellow and green) and $\omega_y = \pm 1$ (red and blue) at $Re = 600$ and $L_y = 6d$ with different spanwise resolutions, (c) $N_y = 72$ nodes and (d) $N_y = 108$ nodes. The center of the plate is located at $x/d = 5.0$ and $z/d = 7.5$.

cells. The subharmonic frequency at $fd/U_0 = 0.2594$ appearing in Fig. 4 is associated with the streamwise vortices, which repeatedly appear at the same spanwise location during alternating shedding cycles.

As the Reynolds number increases beyond 500, the regularity of the vortex structure vanishes. Figure 5 shows the instantaneous vortex formation at $Re = 525$, 550, and 600. It is readily observed (in Figs. 5(a), 5(c), and 5(e)) that the density of streamwise-oriented vortex structures increases with Re . Due to the three-dimensional effects, the spanwise vortex rollers are not parallel to the plate any more. As shown in the instantaneous view of the wake, in Figs. 5(a) and 5(b), at $Re = 525$, and $t = 800$ and $t = 900$, the vortex rollers are tilted. For $Re = 550$ and $t = 900$, in Fig. 5(c),

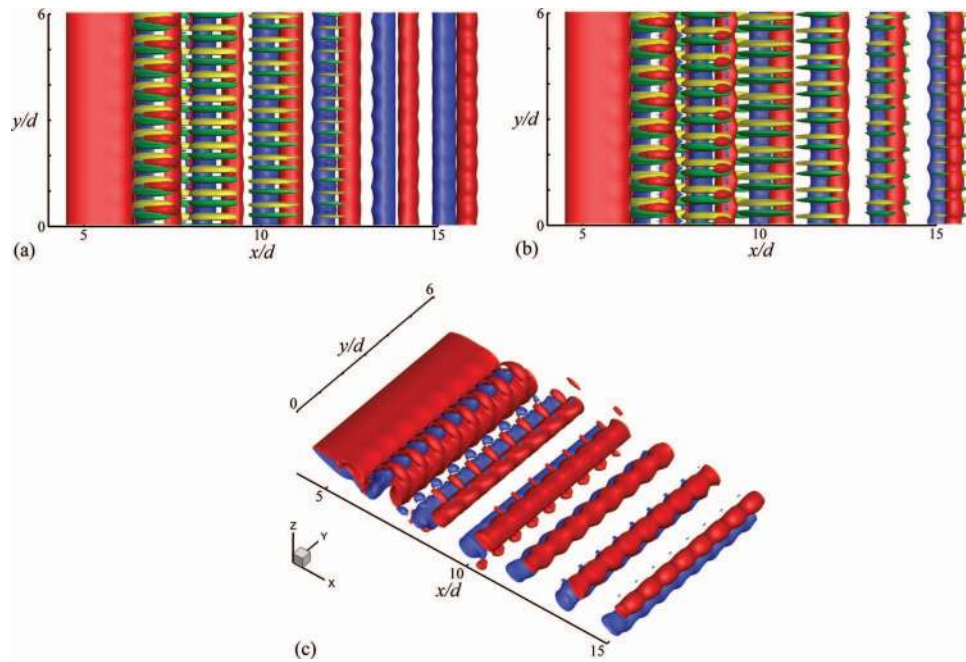


FIG. 2. Instantaneous iso-vorticity surfaces at $t = 500$, $\omega_x = \pm 1$ (yellow and green), and $\omega_y = \pm 1$ (red and blue) at (a) $Re = 450$ and (b) $Re = 500$, and (c) Perspective view of the spanwise vorticity field in the near wake, $\omega_y = \pm 1$ at $Re = 500$.

the vortex rollers exhibit a curved shape in the spanwise direction due to vortex dislocations. Figure 5(d) shows the spanwise iso-vorticity surfaces alone and one can observe that the phase differences are significant. As Re increases to 600, in Fig. 5(e), the wake is more chaotic and the primary vortex rollers are inclined.

Power spectra of the transverse velocity component w at $Re = 525$ are shown in Fig. 6. Multiple peaks, in the range $fd/U_0 = 0.4 - 0.55$ with varying frequency of the dominant peak, are observed along the span. The Fourier analysis provides us with the transformation of the original signal from time to frequency domain, but it is impossible to tell when a particular event takes place.

To illustrate the vortex evolution, Fig. 7 shows the time history of the spanwise vortices and the progressive development of vortex modes at $Re = 550$. The vortex rollers in Figs. 7(a) and 7(b) are

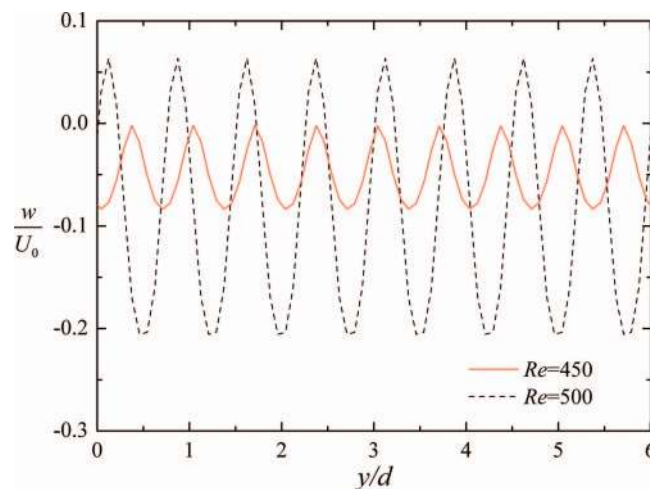


FIG. 3. Spanwise evolution of the instantaneous transverse velocity component w for $Re = 450$ and $Re = 500$, taken at $x/d = 6.0$ and $z/d = 8.0$.

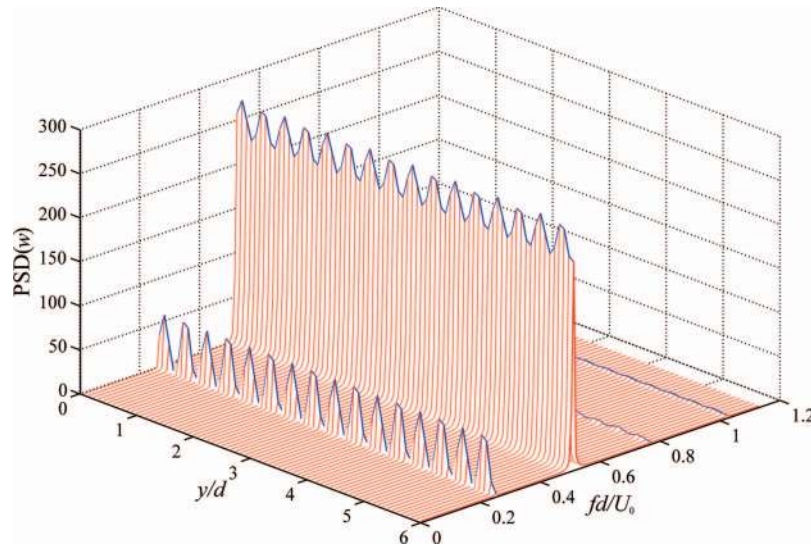


FIG. 4. Spanwise variation of the spectral energy of the transverse velocity component w at $Re = 500$.

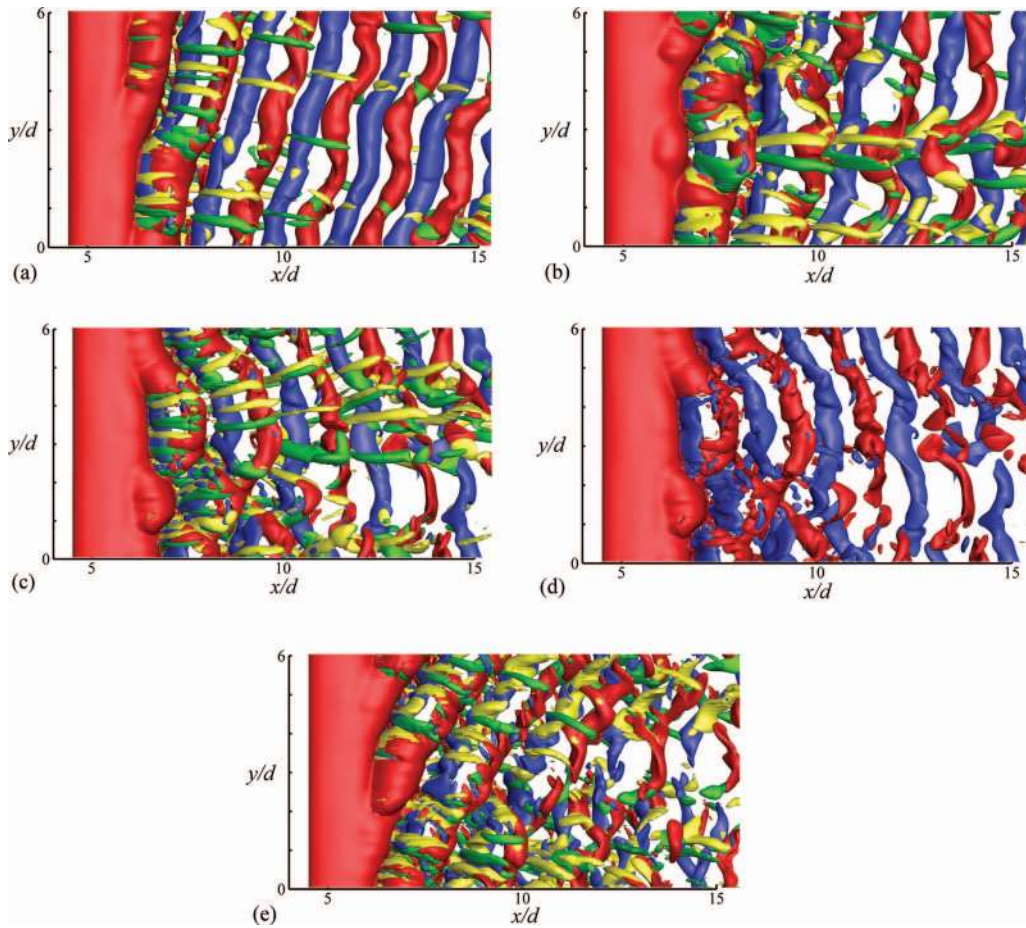


FIG. 5. Instantaneous iso-vorticity surfaces, $\omega_x = \pm 1$ (yellow and green) and $\omega_y = \pm 1$ (red and blue) at (a) $Re = 525$ and $t = 800$, (b) $Re = 525$ and $t = 900$, (c) and (d) $Re = 550$ and $t = 900$, and (e) $Re = 600$ and $t = 900$. t is the dimensionless time.

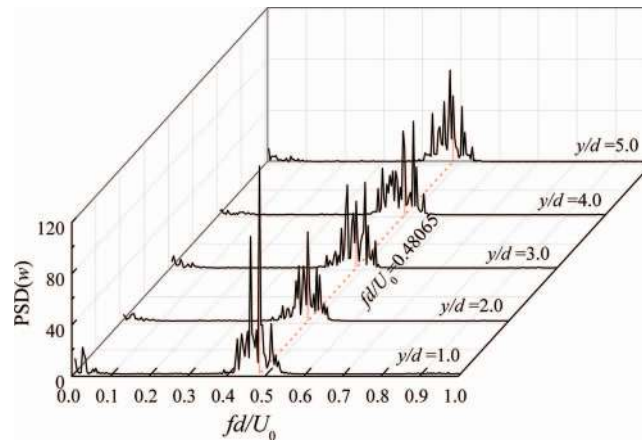


FIG. 6. Power spectra of the transverse velocity component w at selected spanwise locations at $Re = 525$. The time period used is 192 vortex shedding periods. The dotted line, $fd/U_0 = 0.48065$, is the spanwise averaged dominant frequency.

tilted in opposite directions while in Fig. 7(c), almost parallel shedding can be seen in the spanwise range $3 \lesssim y/d \lesssim 5$. The shedding phases are different, however, Figs. 7(d) and 7(e) show a complex shedding process in which the coherence of the primary vortex cells is reduced and substantial three-dimensionalities emerge. Based on this sequence of shedding stages it is found that both oblique and

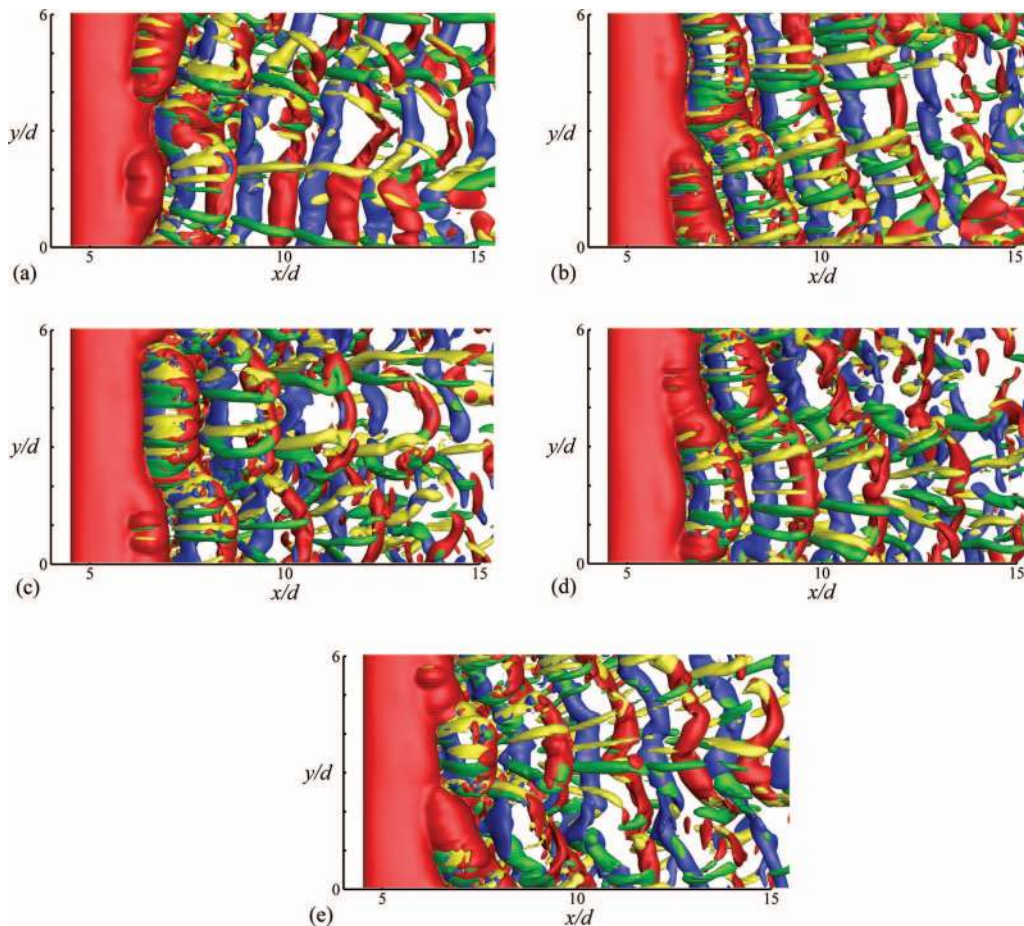


FIG. 7. Instantaneous iso-vorticity surfaces, $\omega_x = \pm 1$ (yellow and green) and $\omega_y = \pm 1$ (red and blue) at $Re = 550$, (a) $t = 500$, (b) $t = 600$, (c) $t = 700$, (d) $t = 800$, and (e) $t = 1000$.

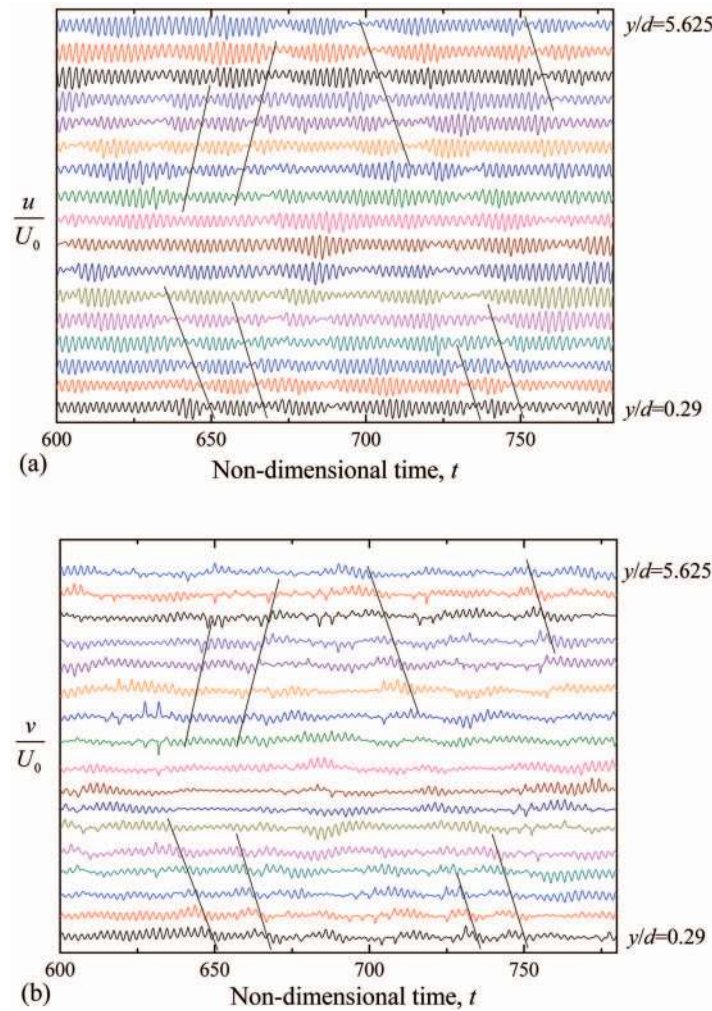


FIG. 8. (a) Streamwise velocity component u and (b) spanwise velocity component v versus time at 17 equidistant y positions along the span at $Re = 550$ ($x/d = 6.0$, $z/d = 8.0$). The straight lines indicate an amplitude decrease or increase.

parallel shedding modes exist. Moreover, as shown in the time dependent evolution of the velocity components u and v in Figs. 8(a) and 8(b), the flow behaves strongly quasi-periodic accompanied by a beating pattern in between for both the streamwise and spanwise velocity components.

The phenomena observed in the present study are similar to observations made in the previous low Reynolds number flow studies (Yang *et al.*¹² and Lewis and Gharib¹⁸) in the wake of a circular cylinder. If the oblique and parallel shedding modes both exist, two slightly different frequencies in the frequency domain and a beating pattern in the time series of the flow variables will be observed. In the previous investigation of vortex shedding in a turbulent wake behind a circular cylinder, Prasad and Williamson³⁷ associated the appearance of a vortex dislocation with a switch between oblique and parallel shedding modes of the von Kármán rollers. In Fig. 8(a), we can see that the amplitude of the u component sometimes decreases considerably. Corresponding to this decrease, the v component increases at the same time. In Fig. 8 these variations are indicated with straight lines. According to Braza *et al.*,³⁸ these large-scale irregular velocity fluctuations among quasi-periodic regions are associated with the vortex dislocation phenomenon. The events detected in the present study describe naturally occurring vortex dislocations. Further evidence of the vortex dislocations will be addressed in the discussion below.

The overall time-dependent evolution of the spanwise flow structure can be seen in Fig. 9, in which the transverse velocity component w is shown as a function of spanwise location and time.

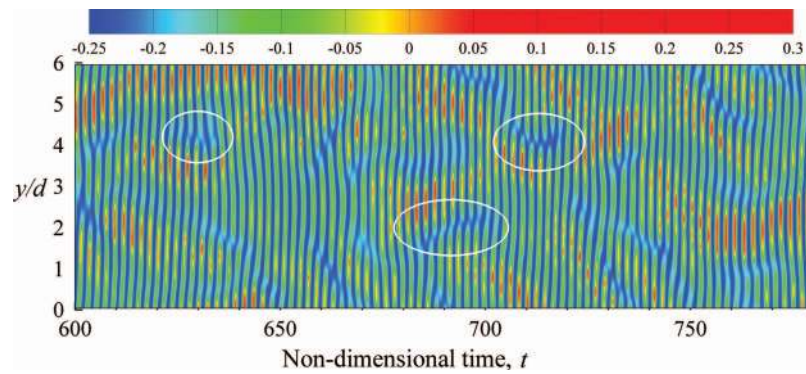


FIG. 9. Transverse velocity component w as a function of time, along span at location $x/d = 6.0$, $z/d = 8.0$ for $Re = 550$. Some of the vortex splittings are indicated by ellipses.

It is shown that periods of oblique and parallel shedding alternate randomly and vortex dislocations appear irregularly.

In Fig. 10, the time series of the streamwise velocity fluctuation $(u - \bar{u}) / U_0$ measured along the span at $x/d = 6.0$, $z/d = 8.0$ for $Re = 550$ is shown. It shows the same pattern as in Fig. 9 in the time period of 650–700. Oblique and parallel shedding modes occur simultaneously over the span. For example, around time $t = 680$, vortices are shed obliquely with both positive and negative phase differences for $y/d < 4.0$ and in parallel for $y/d > 4.0$. In Fig. 10, around time $t = 660$, two vortex roller splittings occur at the same time. These are characterized by decrease and increase of the amplitude of fluctuations in streamwise and spanwise velocity components, respectively, as shown in Fig. 8. The vortex roller splittings describe the natural occurrence of vortex dislocations which appear more frequently at the junctions between the oblique and parallel shedding.

The spectra of the transverse velocity w at $Re = 550$ are shown in Fig. 11(a). First of all it is observed that the fundamental frequency varies along the span. Multiple peaks appear at some spanwise positions. At almost all locations, however, a spectral peak coincides with the spanwise-averaged fundamental frequency $fd / U_0 = 0.4768$. From the perspective view of the spectral energy variation in Fig. 12, it is more clearly seen that the spectral energy of the fundamental frequency is not constant along the span. The spectral energy reduces considerably in some regions. Braza *et al.*³⁸ associated this energy decrease with the appearance of vortex dislocations. They found that less energetic frequency peaks appeared in the vicinity of the fundamental frequency and these peak amplitudes became more pronounced at the spanwise position where the vortex dislocation

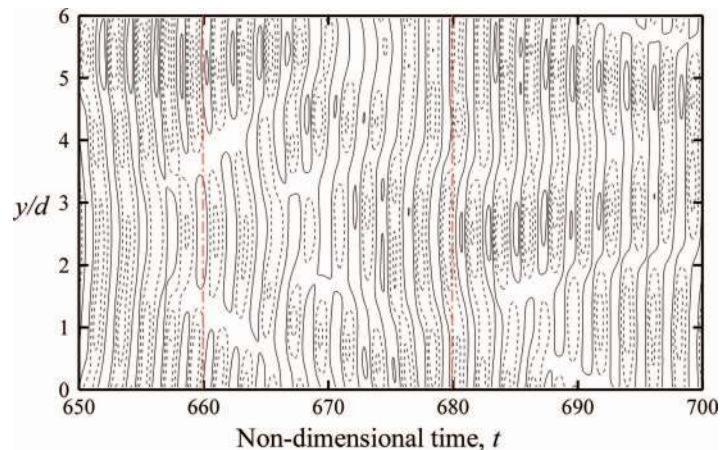


FIG. 10. Time history of streamwise velocity fluctuation $(u - \bar{u}) / U_0$ along the span at location $x/d = 6.0$, $z/d = 8.0$ for $Re = 550$. The solid and dotted contour lines indicate positive and negative values, respectively.

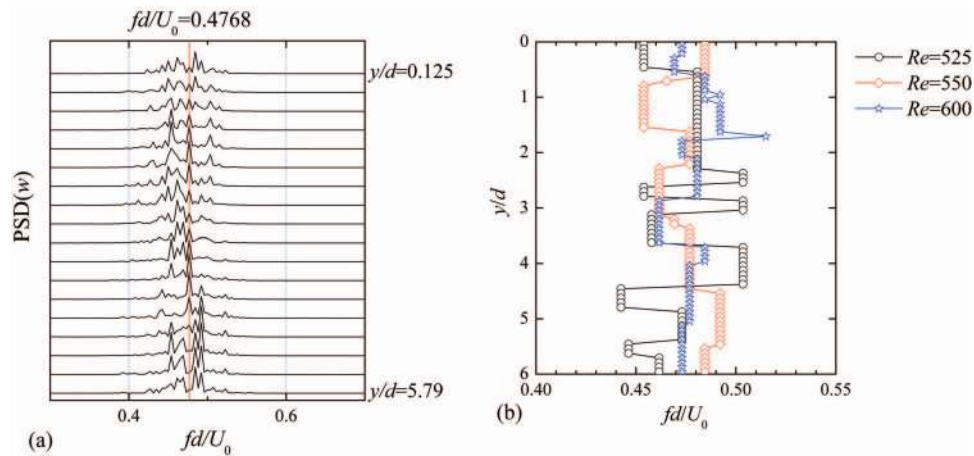


FIG. 11. (a) Spectra of transverse velocity component w along the span at $Re = 550$ and (b) dominant frequency for different Reynolds numbers. The signal tracing time corresponds approximately to 190 vortex shedding periods. The spanwise separation of the spectra in (a) is $\Delta y = 0.33d$.

occurred. The predominant frequency at some different Reynolds numbers is shown in Fig. 11(b). The frequency variation reduces as the Reynolds number increases. This is an obvious effect of the enhanced complexity of the vorticity field at higher Re (see Fig. 5) and the excess three-dimensional scrambling.

In the present study the vortex dislocations appear randomly as shown in Fig. 9. The low energy regions in Fig. 12 correspond to the multiple peak regions in Fig. 11(a). In these regions the frequency peaks scatter over a large frequency range. By comparing the present results with the observation in Braza *et al.*,³⁸ it is found that in the time period in which the frequency spectral energy is analyzed, vortex dislocations appear more frequently in the low energy regions.

B. Wavelet analysis

In addition to the spectral analysis, wavelet transformation (WT) is employed in this study to better understand the instantaneous behavior of the measured velocity signals. At a time instant t , a maximum frequency f_{\max} and the corresponding wavelet coefficient $W(f_{\max}, t)$ can be obtained.

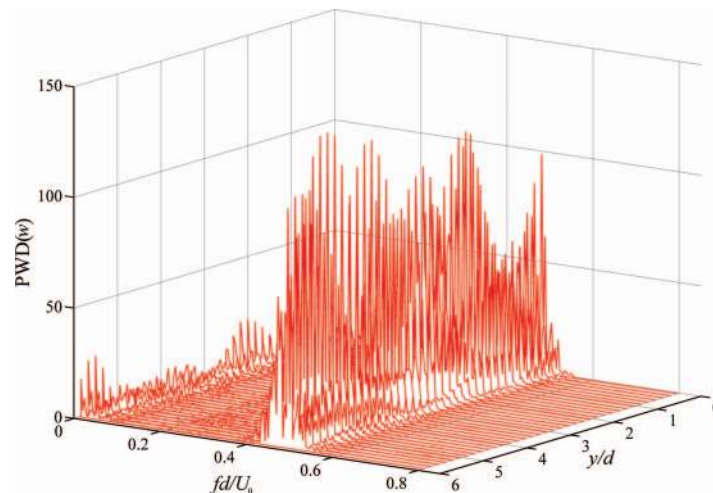


FIG. 12. A perspective view of the spectral energy variations in the spanwise direction at $Re = 550$. The signal's tracing time corresponds approximately to 190 vortex shedding periods.

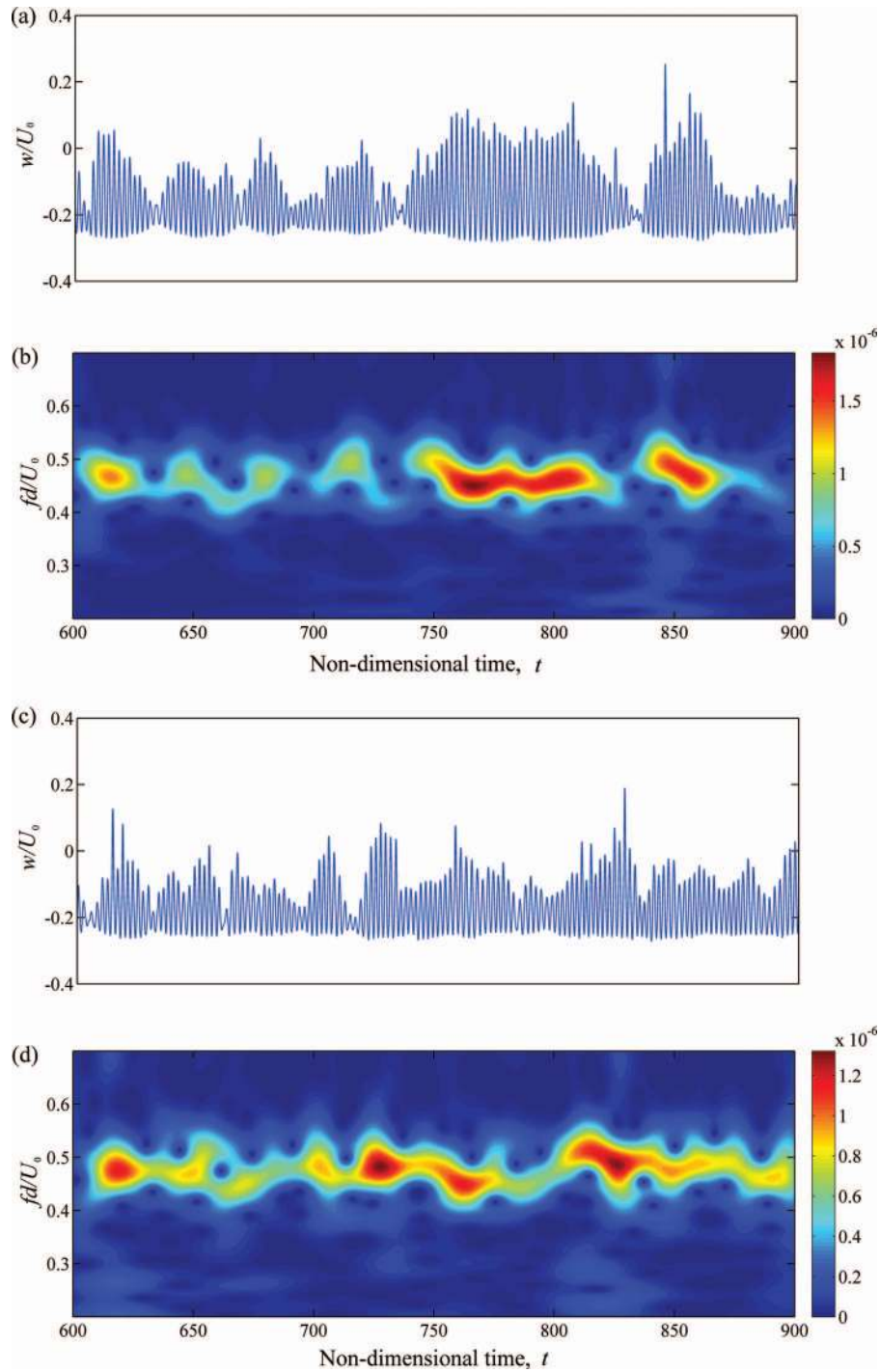


FIG. 13. Wavelet analysis of the transverse velocity w signal at (a) and (b) $x/d = 6.0$, $y/d = 2.0$, $z/d = 8.0$, and (c) and (d) $x/d = 6.0$, $y/d = 4.0$, $z/d = 8.0$ for $Re = 550$. (a) and (c) velocity, (b) and (d) wavelet map.

The amplitude of the vortex shedding frequency is denoted as

$$A(t) = |W(f_{\max}, t)|. \quad (3)$$

For the frequency f at a given time instant t , its phase $\theta(f, t)$ can be further defined as (Wu *et al.*¹⁷)

$$\theta(f, t) = \tan^{-1} \frac{\text{R}(W(f, t))}{\text{I}(W(f, t))}, \quad (4)$$

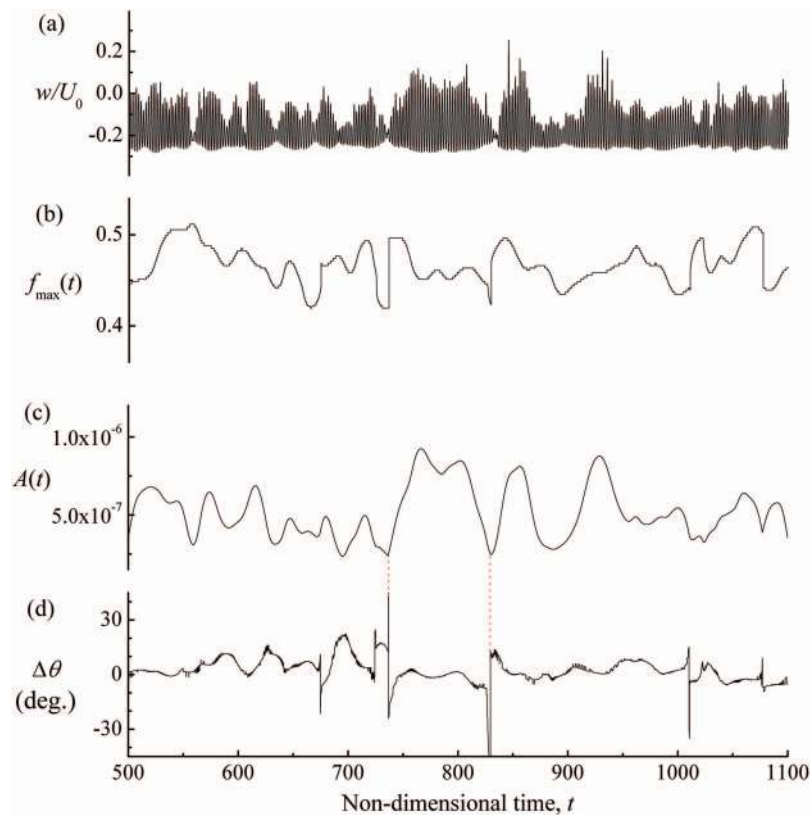


FIG. 14. (a) The w velocity signal at $x/d = 6.0$, $y/d = 2.0$, $z/d = 8.0$ for $Re = 550$, (b) the $f_{\max}(t)$ curve corresponding to the signal trace, (c) the $A(t)$ curve corresponding to maximum frequency $f_{\max}(t)$, and (d) the phase difference of frequency corresponding to two adjacent grid points at $y/d = 2.0$.

in which R and I represent the real and imaginary parts of $W(f, t)$. Consequently, a phase function corresponding to $f_{\max}(t)$ can be defined as $\theta(f_{\max}, t)$. The maximum frequency at a time instant and its amplitude, and the vortex shedding phase, are also obtainable by wavelet transform. The vortex shedding phase is obtained by taking the arctangent of the real and imaginary parts of the wavelet coefficients, which have the highest amplitude in the wavelet maps (see Eq. (4)).

The wavelet analysis provides us with the distribution of the energy density on the frequency versus time map. Two sets of results at spanwise position $y/d = 2.0$ and $y/d = 4.0$ at $Re = 550$, are shown in Fig. 13. At these two positions, the signal modulations are very strong, as shown in Figs. 13(a) and 13(c). These velocity signals are related to the organized coherent motion. The corresponding wavelet maps contain amplitude peaks which display high density (dark red) at the dominant frequencies, in Figs. 13(b) and 13(d). The dark red areas in the wavelet map are not continuous in time. The vortex dislocations occur between the red areas. The wavelet maps show that the frequencies vary with time in the range of 0.4–0.6, especially at the time instant when the vortex dislocations occur.

Figures 14(a) and 15(a) show the transverse velocity signals at the spanwise positions $y/d = 2.0$ and $y/d = 4.0$, respectively, for a time period approximately equivalent to 280 shedding periods. The maximum frequency $f_{\max}(t)$ curves of the two sets of signals are given in Figs. 14(b) and 15(b). The corresponding amplitude $A(t)$ curves are given in Figs. 14(c) and 15(c). The phase differences $\Delta\theta(t)$ shown in Figs. 14(d) and 15(d) are taken from the two sets of signals. The frequency and its amplitude variations at two neighboring grid points (not shown here) are almost indistinguishable. Nevertheless, the vortex shedding phase differences are apparent from both figures in Figs. 14(d) and 15(d). The vertical dotted lines at non-dimensional time $t \approx 740$ and $t \approx 830$ in Figs. 14(c) and 14(d) indicate that a local minimum in $A(t)$ and a strong local phase shift coincides.

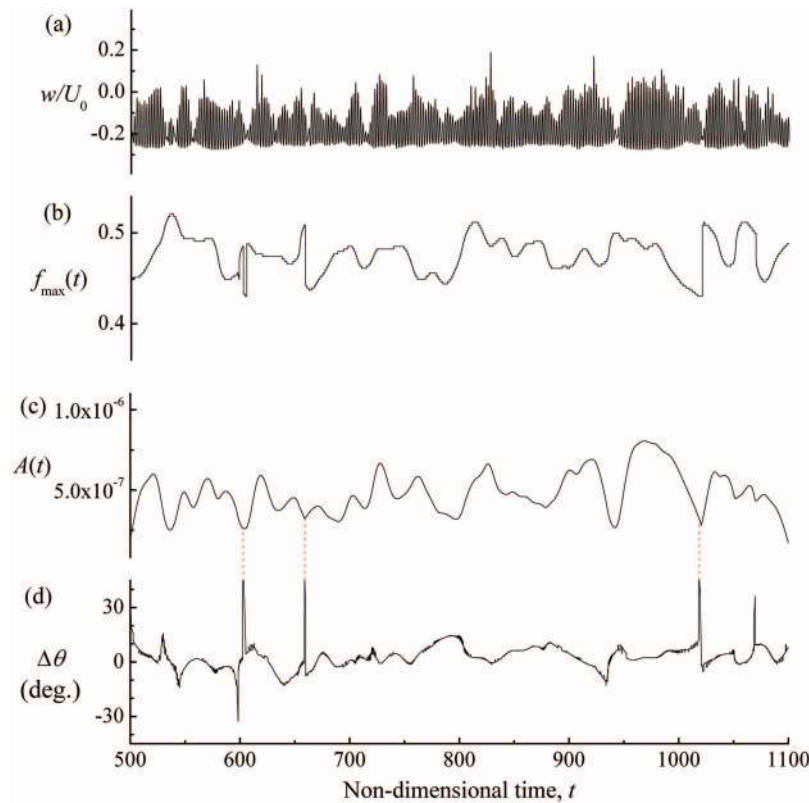


FIG. 15. (a) The w velocity signal at $x/d = 6.0$, $y/d = 4.0$, $z/d = 8.0$ for $Re = 550$. (b) the $f_{\max}(t)$ curve corresponding to the signal trace, (c) the $A(t)$ curve corresponding to maximum frequency $f_{\max}(t)$, and (d) the phase difference of frequency corresponding to two adjacent grid points at $y/d = 4.0$.

The same phenomenon could also be observed at $y/d = 4.0$, as indicated by the vertical dotted lines in Figs. 15(c) and 15(d).

Figure 16 provides an overview of the appearance of the vortex dislocations in a spatio-temporal map. The occurrence of vortex dislocations in the w velocity component is consistent with the vortex shedding phase taken from the wavelet analysis. The phase changes gradually along the span but as the vortex dislocations occur the discontinuities appear also on the phase map. As shown in Fig. 16, at around $t = 900$, vortex dislocations are observed consistently with the vortex structure in Fig. 5(c).

All the results presented so far have been obtained for the $6d$ long plate. However, the use of periodic rather than no-slip boundary conditions at the sidewalls of the computational domain aims to mimic an infinitely long plate, i.e., $L_y/d \rightarrow \infty$. Indeed, the computed drag and lift coefficients reported in Table I became only about 1% lower when the plate length L_y was increased by 50% from $6d$ to $9d$ with exactly the same grid resolution. In order to further examine the role of the plate length, two-point correlation coefficients R_{ij} for the three velocity components are shown in Fig. 17. For the $L_y = 6d$ case shown in Fig. 17(a), the spanwise velocity decorrelates rapidly and R_{vv} attains appreciable negative values for a spanwise separation $\Delta y \approx 1.1d$. This reflects that the spanwise velocity fluctuations tend to be negatively correlated at locations $1.1d$ apart. This distance is significantly larger than the scale of the streamwise vortex structures shown, for instance, in Fig. 7. However, this separation distance is close to half of the wavelength $2.0d$ of the mode B instability reported by Thompson *et al.*²⁸ for the wake behind normal and inclined flat plates. At maximum separation $\Delta y = 3.0d$, $R_{vv} \approx 0$ and no correlation exists. The two-point correlations of the two other velocity components decay gradually with increasing separation distances and attain a modest negative correlation $R_{uu} \approx R_{ww} \approx -0.05$ at maximum separation. This is probably due to a slightly too short plate which is believed to be of marginal influence on the results presented so

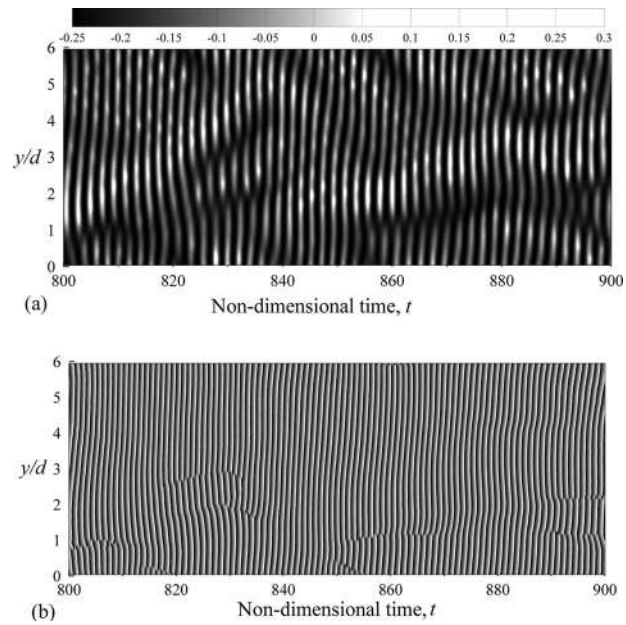


FIG. 16. (a) Transverse velocity component w and (b) vortex shedding phase time series, along span at location $x/d = 6.0$, $z/d = 8.0$ for $Re = 550$.

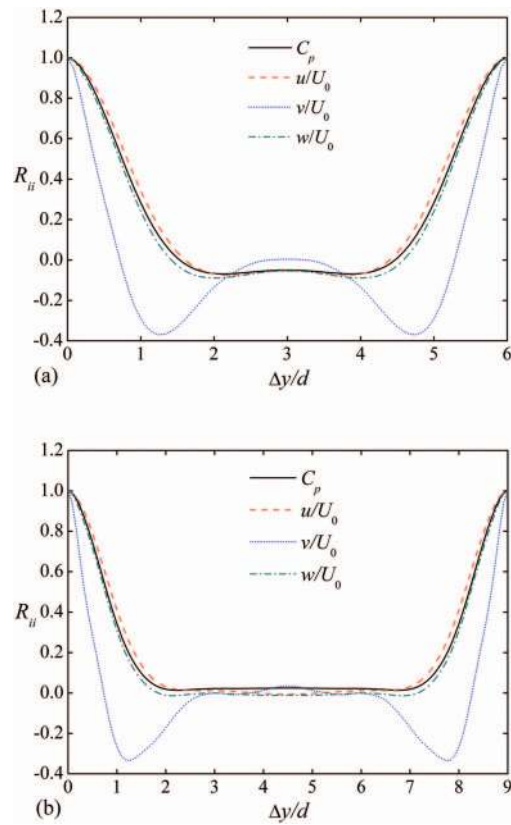


FIG. 17. Two-point correlations in the spanwise direction at $x/d = 6.0$, $z/d = 8.0$ and $Re = 550$. (a) $L_y = 6d$ and (b) $L_y = 9d$.

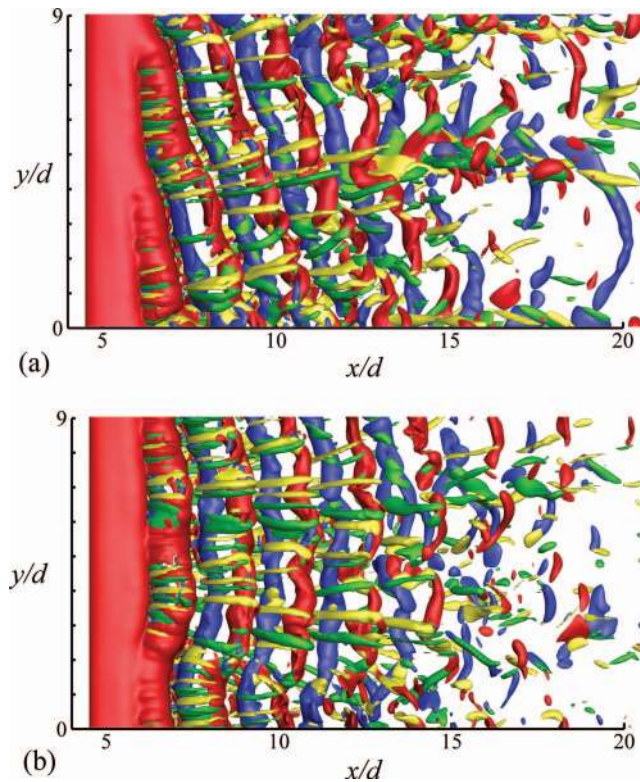


FIG. 18. Instantaneous iso-vorticity surfaces $\omega_x = \pm 1$ (yellow and green) and $\omega_y = \pm 1$ (red and blue) for $Re = 550$ and $L_y = 9d$ (a) $t = 500$ and (b) $t = 700$.

far. The corresponding two-point correlation functions for the case with $L_y = 9d$ are shown in Fig. 17(b). All the three velocity components are now completely decorrelated at separation distances Δy larger than $3.0d$.

Snapshots of the instantaneous vorticity field for the $L_y = 9d$ case are presented in Fig. 18. The Reynolds number and the grid resolution are identical with those in the $L_y = 6d$ case. The plots in Fig. 18 are in all aspects equivalent with the instantaneous plots from the $L_y = 6d$ simulation already shown in Fig. 7. It is particularly noteworthy that the primary vortex shedding also here alternates between parallel and oblique shedding modes. The spontaneous occurrences of vortex dislocations

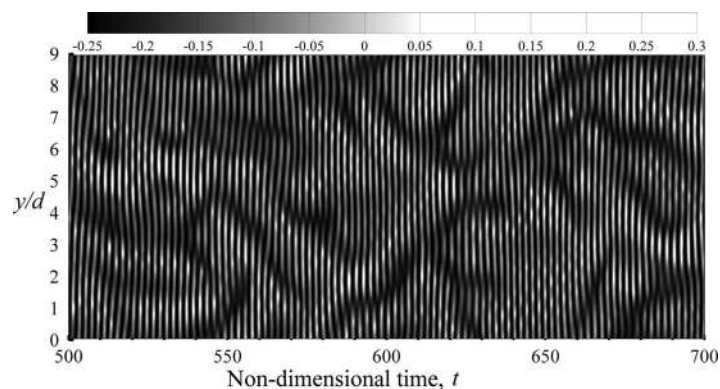


FIG. 19. Transverse velocity component w time series, along span at location $x/d = 6.0$, $z/d = 8.0$ for $Re = 550$ and $L_y = 9d$.

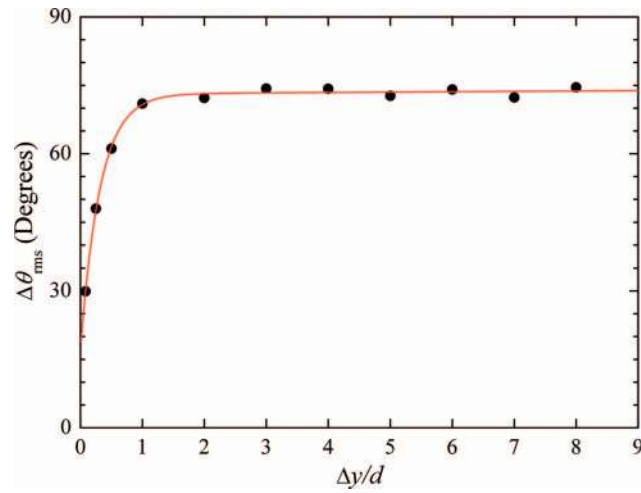
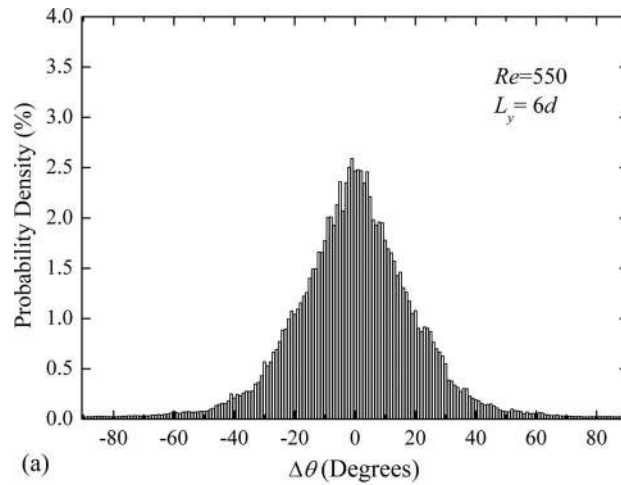
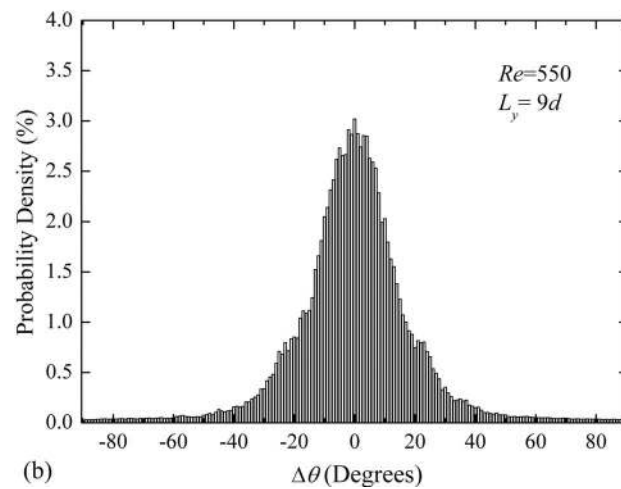


FIG. 20. Fluctuating phase difference between two signals with increasing spanwise separation, at $Re = 550$ and $L_y = 9d$. The solid line is an exponential curve fit of Eq. (5) with coefficients $A = 73.11$, $B = 0.00112$, $C = -55.98$, and $D = -3.141$.



(a)



(b)

FIG. 21. Probability density function of phase differences $\Delta\theta$ with the spanwise separation $\Delta y/d = 0.25$ at $Re = 550$. The signals are taken from $x/d = 6.0$, $z/d = 8.0$ for a time period of 280 and 140 shedding cycles for the two cases, respectively, (a) $L_y = 6d$ and (b) $L_y = 9d$.

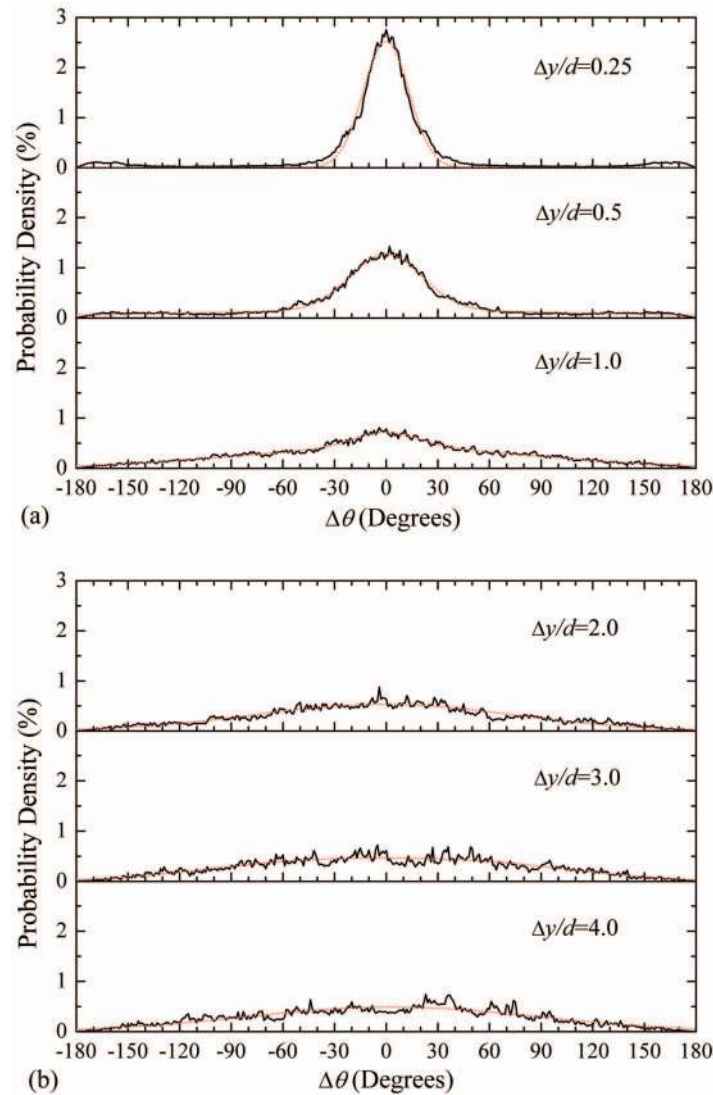


FIG. 22. Probability density function of phase differences for different spanwise separations at $Re = 550$. The signals are taken from $x/d = 6.0$, $z/d = 8.0$, (a) $\Delta y/d = 0.25$, $\Delta y/d = 0.5$, and $\Delta y/d = 1.0$ and (b) $\Delta y/d = 2.0$, $\Delta y/d = 3.0$, and $\Delta y/d = 4.0$. The dotted lines are the Gaussian distributions with the same standard deviation.

in the time traces of the transverse velocity component w in Fig. 19 are also in complete accordance with the corresponding time series from the $L_y = 6d$ case shown in Fig. 16.

C. Spanwise phase difference

In Subsection III B, it has been shown that oblique and parallel vortex sheddings co-exist in the wake. The vortex dislocations appear more often at the junction of these two shedding modes. In the present subsection, the phase difference resulting from the oblique shedding and vortex dislocations are calculated from the $L_y = 9d$ case. For this particular purpose, this will provide more accurate statistical results than the $L_y = 6d$ case. The phase differences are taken from the spanwise locations with separations ranging from $\Delta y/d = 0.25$ to $\Delta y/d = 8.0$. Calculations were carried out by crossing the span starting at either side in order to avoid bias. The results of the analysis are summarized in the form of the root-mean-square (RMS) values and probability density functions (PDFs) of the phase differences.

Figure 20 shows the fluctuating (RMS) phase difference $\Delta\theta_{\text{rms}}$ with increasing spanwise separations. This is a measure of the efficiency of the three-dimensionalization of the wake. There seems to be a continuous increase of the phase difference for increasing separation up to $\Delta y/d = 1.0$. For $\Delta y/d > 2.0$, $\Delta\theta_{\text{rms}}$ approaches asymptotically to an angle of $\sim 74^\circ$. The solid curve is an exponential fit to the data points:

$$\Delta\theta_{\text{rms}} = A \exp [B (\Delta y/d)] + C \exp [D (\Delta y/d)]. \quad (5)$$

This is consistent with the two-point correlations in Fig. 17(b) which showed that the streamwise and transverse velocity fluctuations became decorrelated for spanwise separations $\Delta y \gtrsim 2.0d$.

Figures 21 and 22 show the PDF of the phase difference $\Delta\theta$ along the span. In Fig. 21, the PDFs for $L_y = 6d$ and $L_y = 9d$ with $\Delta y/d = 0.25$ are plotted. The histograms for $\Delta y/d = 0.25$ both exhibit a sharp peak and nearly symmetric probability distribution with respect to $\Delta\theta = 0$. The phase differences along the span over a time period of 140 shedding cycles have a zero mean. These events indicate that the contributions from the positive and negative phase differences are equal. In Fig. 22(a), the curves for $\Delta y/d = 0.25$, $\Delta y/d = 0.5$, and $\Delta y/d = 1.0$ (solid lines) are plotted as well as the corresponding Gaussian distributions (dotted lines) with the same standard deviation. The curves for $\Delta y/d = 2.0$, $\Delta y/d = 3.0$, and $\Delta y/d = 4.0$, in Fig. 22(b), show similar density distributions but with larger fluctuations as $\Delta y/d$ increases. It is readily seen that the standard deviation of the PDFs increases monotonically with increasing separation $\Delta y/d$ up till $\Delta y/d = 2.0$ and the distributions in Fig. 22(a) therefore appear to broaden. As the separation is further increased, however, the PDFs in Fig. 22(b) are only modestly changed. This is consistent with the variation of $\Delta\theta_{\text{rms}}$ in Fig. 20 which suggested that separations greater than $2.0d$ do not alter the phase differences. In spite of the increasing separation Δy in the different plots in Fig. 22, all distributions appear as almost Gaussian and centered with the peak at $\Delta\theta = 0$. Due to the normalization, the actual peak value is inevitably reduced as the standard deviation becomes larger.

IV. CONCLUSIONS

In the present paper results from three-dimensional simulations of the vortex shedding behind an inclined flat plate at 20° angle of attack have been presented and analyzed with the view to find out whether or not oblique vortex shedding occurs in the range of Reynolds numbers from 400 to 600. The investigation was motivated by our unexpected observation that oblique shedding occurred at $\alpha = 20^\circ$ and $Re = 1000$; see Yang *et al.*²⁹ It was first observed that only parallel shedding took place in the Reynolds number range 400–500 although the wake became distinctly three-dimensional with organized pairs of counter-rotating streamwise vortices or so-called “braids” which connect the primary von Kármán vortex cells. In the Re -interval from 525 to 600, on the other hand, oblique vortex shedding was observed, similarly as in the $Re = 1000$ case considered by Yang *et al.*²⁹ Their conjecture that this intrinsic instability was associated with the particular angle of incidence rather than the Reynolds number has therefore been confirmed.

Frequency analysis showed multiple spectral peaks as well as an amplitude variation along the span. The time histories of the velocity components in the wake region indicated that oblique and parallel sheddings co-exist in the wake. Vortex dislocations arise at the locations where the instantaneous flow field abruptly switches from parallel to oblique modes of shedding. A beating pattern in the velocity signals also reflects vortex splitting.

A wavelet analysis provides another manifestation of the irregular variation of the local frequency of the amplitude peaks in time. Phase differences between signals at different spanwise locations are obtained from the phase function of the amplitude peaks in the frequency map. The standard deviation of the phase difference increases monotonically with increasing spanwise separations Δy up to 74° and thereafter remains constant for separations larger than $2.0d$. The probability distributions of the phase difference remain closely Gaussian and centered about zero. This observation strongly suggests that positive and negative inclinations of the obliquely shed vortex cell are of equal likelihood.

ACKNOWLEDGMENTS

This work has received support from the Research Council of Norway (Program for Supercomputing) through a grant of computing time.

- ¹ A. Roshko, "Perspective on bluff body aerodynamics," *J. Wind Eng. Ind. Aerodyn.* **49**, 79 (1993).
- ² H. Eisenlohr and H. Eckelmann, "Vortex splitting and its consequences in the vortex street wake of cylinders at low Reynolds number," *Phys. Fluids A* **1**, 189 (1989).
- ³ C. H. K. Williamson, "Oblique and parallel modes of vortex shedding in the wake of a circular cylinder at low Reynolds numbers," *J. Fluid Mech.* **206**, 579 (1989).
- ⁴ C. H. K. Williamson, "Defining a universal and continuous Strouhal-Reynolds number relationship for the laminar vortex shedding of a circular cylinder," *Phys. Fluids* **31**, 2742 (1988).
- ⁵ S. Behara and S. Mittal, "Flow past a circular cylinder at low Reynolds number: Oblique vortex shedding," *Phys. Fluids* **22**, 054102 (2010).
- ⁶ C. H. K. Williamson, "The existence of two stages in the transition to three dimensionality of a circular cylinder wake," *Phys. Fluids* **31**, 3165 (1988).
- ⁷ C. H. K. Williamson, "The natural and forced formation of spot-like 'vortex dislocations' in the transition of a wake," *J. Fluid Mech.* **243**, 393 (1992).
- ⁸ G. Karniadakis and G. S. Triantafyllou, "Three-dimensional dynamics and transition to turbulence in the wake of bluff objects," *J. Fluid Mech.* **238**, 1 (1992).
- ⁹ D. R. Williams, H. Mansy, and A. Abouel-Fotouh, "Three-dimensional subharmonic waves during transition in the near-wake region of a cylinder," *Phys. Fluids* **8**, 1476 (1996).
- ¹⁰ R. Mittal and S. Balachandar, "Generation of streamwise vortical structures in bluff body wakes," *Phys. Rev. Lett.* **75**, 1300 (1995).
- ¹¹ R. D. Henderson, "Nonlinear dynamics and pattern formation in turbulent wake transition," *J. Fluid Mech.* **352**, 65 (1997).
- ¹² P.-M. Yang, H. Mansy, and D. R. Williams, "Oblique and parallel wave interaction in the near wake of a circular cylinder," *Phys. Fluids* **5**, 1657 (1993).
- ¹³ H. Mansy, P.-M. Yang, and D. R. Williams, "Quantitative measurements of three-dimensional structures in the wake of a circular cylinder," *J. Fluid Mech.* **270**, 277 (1994).
- ¹⁴ J. J. Miao, J. T. Wang, J. H. Chou, and C. Y. Wei, "Characteristics of low-frequency variations embedded in vortex-shedding process," *J. Fluids Struct.* **13**, 339 (1999).
- ¹⁵ J. J. Miao, J. T. Wang, J. H. Chou, and C. Y. Wei, "Low-frequency fluctuations in the near-wake region of a trapezoidal cylinder with low aspect ratio," *J. Fluids Struct.* **17**, 701 (2003).
- ¹⁶ J. J. Miao, S. J. Wu, C. C. Hu, and J. H. Chou, "Low-frequency modulations associated with vortex shedding from flow over bluff body," *AIAA J.* **42**, 1388 (2004).
- ¹⁷ S. J. Wu, J. J. Miao, C. C. Hu, and J. H. Chou, "On low-frequency modulations and three-dimensionality in vortex shedding behind a normal plate," *J. Fluid Mech.* **526**, 117 (2005).
- ¹⁸ C. G. Lewis and M. Gharib, "An exploration of the wake three dimensionalities caused by a local discontinuity in cylinder diameter," *Phys. Fluids* **4**, 104 (1992).
- ¹⁹ F.-B. Hsiao and C. H. Chiang, "Experimental study of cellular shedding vortices behind a tapered circular cylinder," *Exp. Therm. Fluid Sci.* **17**, 179 (1998).
- ²⁰ S. Mittal, "Computation of three-dimensional flows past circular cylinder of low aspect ratio," *Phys. Fluids* **13**, 177 (2001).
- ²¹ V. D. Narasimhamurthy, H. I. Andersson, and B. Pettersen, "Cellular vortex shedding in the wake of a tapered plate," *J. Fluid Mech.* **617**, 355 (2008).
- ²² V. D. Narasimhamurthy, H. I. Andersson, and B. Pettersen, "Cellular vortex shedding behind a tapered circular cylinder," *Phys. Fluids* **21**, 044106 (2009).
- ²³ G. C. Ling and H. L. Zhao, "Vortex dislocations in wake-type flow induced by spanwise disturbances," *Phys. Fluids* **21**, 073604 (2009).
- ²⁴ C. Morton and S. Yarusevych, "Vortex shedding in the wake of a step cylinder," *Phys. Fluids* **22**, 083602 (2010).
- ²⁵ Z. Y. Huang, V. D. Narasimhamurthy, and H. I. Andersson, "Oblique and cellular vortex shedding behind a circular cylinder in a bidirectional shear flow," *Phys. Fluids* **22**, 114105 (2010).
- ²⁶ W. Dunn and S. Tavoularis, "Vortex shedding from a step-cylinder in spanwise sheared flow," *Phys. Fluids* **23**, 035109 (2011).
- ²⁷ S. C. C. Bailey, R. J. Martinuzzi, and G. A. Kopp, "The effects of wall proximity on vortex shedding from a square cylinder: Three-dimensional effects," *Phys. Fluids* **14**, 4160 (2002).
- ²⁸ M. C. Thompson, K. Hourigan, K. Ryan, and G. J. Sheard, "Wake transition of two-dimensional cylinders and axisymmetric bluff bodies," *J. Fluids Struct.* **22**, 793 (2006).
- ²⁹ D. Yang, B. Pettersen, H. I. Andersson, and V. D. Narasimhamurthy, "Vortex shedding in flow past an inclined flat plate at high incidence," *Phys. Fluids* **24**, 084103 (2012).
- ³⁰ K. M. Lam and M. Y. H. Leung, "Asymmetric vortex shedding flow past an inclined flat plate at high incidence," *Eur. J. Mech. B/Fluids* **24**, 33 (2005).
- ³¹ A. E. Perry and T. R. Steiner, "Large-scale vortex structures in turbulent wakes behind bluff bodies. Part 1. Vortex formation processes," *J. Fluid Mech.* **174**, 233 (1987).
- ³² M. Manhart, "A zonal grid algorithm for DNS of turbulent boundary layers," *Comput. Fluids* **33**, 435 (2004).
- ³³ H. L. Stone, "Iterative solution of implicit approximations of multidimensional partial differential equations," *SIAM J. Numer. Anal.* **5**, 530 (1968).

- ³⁴N. Peller, A. L. Duc, F. Tremblay, and M. Manhart, "High-order stable interpolations for immersed boundary methods," [Int. J. Numer. Methods Fluids](#) **52**, 1175 (2006).
- ³⁵D. Yang, V. D. Narasimhamurthy, B. Pettersen, and H. I. Andersson, "Three-dimensional wake transition behind an inclined flat plate," [Phys. Fluids](#) **24**, 094107 (2012).
- ³⁶M. Breuer and N. Jovičić, "Separated flow around a flat plate at high incidence: an LES investigation," [J. Turbulence](#) **2**, 018 (2001).
- ³⁷A. Prasad and C. H. K. Williamson, "Three-dimensional effects in turbulent bluff-body wakes," [J. Fluid Mech.](#) **343**, 235 (1997).
- ³⁸M. Braza, D. Faghani, and H. Persillon, "Successive stages and the role of natural vortex dislocations in three-dimensional wake transition," [J. Fluid Mech.](#) **439**, 1 (2001).